

THE FORMATION OF A PROMINENCE IN ACTIVE REGION NOAA 8668. I. *SOHO*/MDI OBSERVATIONS OF MAGNETIC FIELD EVOLUTION

JONGCHUL CHAE,^{1,2} HAIMIN WANG,¹ JIONG QIU,¹ PHILIP R. GOODE,¹ LOUIS STROUS,³ AND H. S. YUN⁴

Received 2001 February 22; accepted 2001 June 13

ABSTRACT

We have studied the evolution of the photospheric magnetic field in active region NOAA 8668 for 3 days while the formation of a reverse S-shaped filament proceeded. From a set of full-disk line-of-sight magnetograms taken by the Michelson Doppler Imager (MDI) on board the *Solar and Heliospheric Observatory (SOHO)*, we have found a large canceling magnetic feature that was closely associated with the formation of the filament. The positive flux of the magnetic feature was initially 1.5×10^{21} Mx and exponentially decreased with an e -folding time of 28 hr throughout the period of observations. We also have determined the transverse velocities of the magnetic flux concentrations in the active region by applying local correlation tracking. As a result, a persistent pattern of shear motion was identified in the neighborhood of the filament. The shear motion had a speed of $0.2\text{--}0.5$ km s⁻¹ and fed negative magnetic helicity of -3×10^{42} Mx² into the coronal volume during an observing run of 50 hr at an average rate of -6×10^{40} Mx² hr⁻¹. This rate is an order of magnitude higher than the rate of helicity change due to the solar differential rotation. The magnetic flux of the field lines created by magnetic reconnection and the magnetic helicity generated by the photospheric shear motion are much more than enough for the formation of the filament. Based on this result, we conjecture that the filament formation may be the visible manifestation of the creation of a much bigger magnetic structure that may consist of a flux rope and an overlying sheared arcade.

Subject headings: Sun: filaments — Sun: magnetic fields — Sun: photosphere — Sun: prominences

1. INTRODUCTION

Solar prominences—and equivalently, filaments—are dense chromospheric plasma suspended in the solar corona by highly nonpotential magnetic field. The formation of prominences has been one of the challenging problems in solar research. It was observationally established several decades ago that prominences are located above photospheric boundaries separating between opposite-polarity magnetic fields. More recent observations relevant to the formation of prominences were reviewed by Martin (1998). But how the formation of a prominence proceeds has rarely been studied observationally, mainly because of the difficulty of performing high-quality uninterrupted observations of prominences under formation.

Theoretical studies have suggested that the formation of a prominence may be a consequence of restructuring of coronal magnetic fields driven by photospheric flow. Two kinds of photospheric flow have been considered as the main driver of prominence formation: converging flow and shear flow. Converging flow toward the polarity reversal boundary appears to be important since it can cause opposite-polarity magnetic fields to collide and subsequently drive magnetic reconnection—an efficient way of magnetic field restructuring (van Ballegoijen & Martens 1989; Ridgway & Priest 1993; Galsgaard & Longbottom

1999). Converging flow has been reported from observations (Martin 1998). Moreover, flux cancellation—defined by the mutual disappearance of positive magnetic flux and negative magnetic flux—has been frequently observed in association with the formation of a prominence (Martin, Livi, & Wang 1985; Martin 1998).

Flux cancellation is usually interpreted as a manifestation of reconnection in the low atmosphere, particularly in the temperature minimum region (Litvinenko 1999). Van Ballegoijen & Martens (1989) first incorporated canceling magnetic features (CMFs) in modeling the formation of filaments and successfully explained the origin of helical structures observed in prominences. Subsequent theoretical studies also showed that magnetic reconnection in the low atmosphere can effectively drive upward the mass that is required for prominence formation (Litvinenko & Somov 1994; Priest, van Ballegoijen, & Mackay 1996; Galsgaard & Longbottom 1999; Litvinenko & Martin 1999).

The physical nature of observed converging flow, however, is little understood so far. We do not even know whether a converging flow represents an organized large-scale flow or is simply a result of random motion of magnetic concentrations passing the polarity reversal boundary.

Shear flow has been an important input to theoretical models of prominence formation, for it can produce highly sheared magnetic field from initially potential field (van Ballegoijen & Martens 1989; Choe & Lee 1992; DeVore & Antiochos 2000). The nonpotentiality of magnetic field is known to be a necessary condition for filament formation. Filaments are observed to form in the polarity reversal boundary where channels of fibrils run parallel to the polarity reversal boundary (Martin 1998). Since fibrils are field aligned, the existence of such channels implies that the magnetic fields in and around filaments are predominantly

¹ Big Bear Solar Observatory, New Jersey Institute of Technology, 40386 North Shore Lane, Big Bear City, CA 92314.

² Department of Astronomy and Space Science, Chungnam National University, Taejon 305-764, South Korea; chae@cnu.ac.kr.

³ Lockheed Martin Advanced Technology Center, O/L9-41, B/252, 3251 Hanover Street, Palo Alto, CA 94304.

⁴ Astronomy Program, SEES, Seoul National University, 151-742 Seoul, South Korea.

along the polarity reversal boundary and hence are highly nonpotential. Theoretical studies have indicated that nonpotential magnetic fields may have dip structures that can sustain cool plasma against the solar gravity (Choe & Lee 1992).

Despite its physical importance in filament formation, shear flow specific to filament-forming regions has rarely been studied observationally. Solar differential rotation is a kind of shear flow in a filament channel with a polarity reversal boundary that is significantly oriented in the east-west direction. But whether there also exist other kinds of shear flow is an open question to be answered from observations.

In 1999 August, the active region NOAA 8668 was jointly observed by the *Solar and Heliospheric Observatory* (SOHO), the *Transition Region and Coronal Explorer* (TRACE), and the Big Bear Solar Observatory (BBSO) for several days. The active region included a reverse S-shaped filament that was under formation during the period of observations. These observations produced various sets of time-series data of high quality that provide unprecedented opportunities for studying the formation of an active region prominence at different atmospheric levels.

In the present paper, we focus on the evolution of the photospheric magnetic field near the active region prominence during its formation. For this purpose, we will analyze magnetogram data taken by the Michelson Doppler Imager (MDI) on board SOHO. Specifically, we will measure the flux change of a sizeable canceling magnetic feature that was found near the filament. We will also determine the transverse motion of all the magnetic concentrations in the neighborhood of the filament by utilizing local correlation tracking (LCT). As a result, a persistent shear flow will be identified that is different from the solar differential rotation. The effect of the shear flow on the nonpotentiality of the magnetic fields will be evaluated by the rate of change of magnetic helicity due to the flow. Finally, the physical implications of the observed magnetic evolution on the formation of the prominence will be discussed.

2. DATA AND ANALYSIS

2.1. Data

In the present study, we analyze full-disk line-of-sight magnetograms taken by SOHO/MDI. MDI full-disk magnetograms are recorded by its 1024×1024 CCD detector with a pixel size of $2''$. MDI magnetograms have been calibrated by comparing the MDI magnetogram signal to simulated values (Scherrer et al. 1995), and the conversion factor 2.82 G DN^{-1} is commonly used (e.g., Schrijver et al. 1997). There are two kinds of MDI full-disk magnetogram data: 1 minute cadence data and 96 minute cadence data. We used 1 minute cadence data to determine transverse velocities. The noise level in the 1 minute cadence data, which has been determined from a comparison of two successive full-disk magnetograms, is about 17 G pixel^{-1} . The noise level can be reduced by taking averages of several successive magnetograms at the sacrifice of temporal resolution. We also used 96 minute cadence data for the study of hour-to-hour variation of magnetic flux for several days. Magnetograms of 96 minute cadence are averages of five high-rate magnetograms and have a noise level of 7.6 G pixel^{-1} .

2.2. Mapping, Subpixelization, and Time-averaging

Magnetograms taken at different times are aligned based on the nonlinear mapping defined by the differential solar rotation,

$$\omega = 2.894 - 0.428 \sin^2 b - 0.370 \sin^4 b \mu\text{rad s}^{-1} \quad (1)$$

(Howard, Harvey, & Forgach 1990). This rotational mapping is also effective in correcting for the geometrical foreshortening that arises from the spherical geometry of the Sun. The reference time has been chosen to be 1999 August 20 03:00 UT, at which instant the active region passed through the central meridian. We realize the mapping by determining an interpolated value of flux density at every position in the new grids that have a pixel size of $1''$, one-half of the original pixel size in MDI full-disk magnetograms. We employ this subpixelized interpolation to get smooth flux distributions without losing spatial resolution. To increase the signal-to-noise ratio, we also take time averages by integrating seven successive magnetograms with 1 minute cadence. This reduces the noise level down to 6.6 G pixel^{-1} .

2.3. Corrections for Geometrical Effects

If an observed area is away from disk center, the observed line-of-sight flux may become much different from the vertical flux for two reasons. First, the observed area becomes foreshortened. This effect is automatically corrected when rotational mapping to the central meridian is applied. The other reason is that the line-of-sight field strength generally differs from the vertical field strength. For simplicity, we assume that magnetic fields in the photosphere are predominantly vertical. Then the vertical field strength becomes equal to the line-of-sight field strength times $1/\cos \psi$, where ψ is the heliocentric angle of the region. This simple correction appears reasonably good in quiet-Sun networks and active region plages and sunspot umbrae. On the other hand, it may not be satisfactory in sunspot penumbrae and at polarity reversal boundaries where magnetic fields may be more horizontal than vertical, which may limit the accuracy of the correction. The error in the correction depends on the location of the observed area on the solar disk as well as the horizontal field strengths. The explicit formulae of this error on the different observing days are given in Appendix A. Detailed discussion on the possible error of the projection correction will be given later based on these formulae.

2.4. Local Correlation Tracking

In currently available magnetograms of a spatial resolution $1''\text{--}3''$, most of magnetic flux exists on the solar surface in clumps that are often called magnetic flux concentrations or magnetic concentrations. Magnetic concentrations may be clusters of magnetic flux tubes that are known to have a typical size of $0.2''$. We determine the transverse velocities of magnetic concentrations by measuring their relative displacements between two successive magnetograms using the technique of local correlation tracking (November & Simon 1988). The transverse velocities in the regions of very low flux density are suppressed to zero since they may be strongly subject to noise and may not represent the real velocities of magnetic concentrations.

There are two important parameters in LCT that have to be properly chosen: the FWHM of the apodizing function and the time interval between the two images to be com-

pared. An optimal value of the FWHM of the apodizing function should be bigger than the size of the smallest features seen in the data. We choose an FWHM of $8''$, 2 times the spatial resolution of the MDI full-disk magnetograms. The time interval between two successive images is constrained by the requirement that physically significant displacements should be large enough to be well determined by the LCT (greater than, for example, 0.1 pixel ≈ 70 km) and, at the same time, should be much smaller than the apodizing window size ≈ 6000 km. Physically significant transverse velocities of photospheric fluxes are less than 1.5 km s^{-1} , and we choose a time interval of 20 minutes.

Note that LCT is applied to magnetograms that have been corrected for solar rotation. Therefore, the transverse velocities determined by LCT do not include solar rotation. The solar rotational velocity can be independently computed from equation (1). The velocity varies from 1.64 to 1.93 km s^{-1} in the latitudinal zone $14^\circ < b < 31^\circ$ where NOAA 8668 was located during the period of our observations.

The LCT technique was originally applied to track intensity patterns such as granulation, in which case the intensity variation in space and time may produce artifacts in the measured velocities. On the other hand, LCT applied to magnetograms is very little subject to such artifacts since the timescale of significant change of the magnetic signal is longer (\geq a few hr) than the time interval of two successive magnetograms (20 minutes).

LCT applied to magnetograms away from the disk center may be subject to an error since the error in projection correction may systematically change with time because of solar rotation. This kind of error is serious where the error of projection correction is large—where transverse magnetic fields dominate vertical magnetic fields. We have presented the expressions for such spurious velocity in Appendix B, and we will discuss this problem in the results section.

2.5. Determination of Magnetic Helicity Change Rate

Photospheric motion is a way of changing magnetic helicity in the solar corona. According to Berger (1999) and Priest & Forbes (2000), the rate of magnetic helicity change of the coronal volume due to the shuffling of footpoints on the surface S is given by

$$\frac{dH}{dt} = -2 \oint_S (\mathbf{v} \cdot \mathbf{A}_p) B_z dS, \quad (2)$$

where \mathbf{A}_p is the vector potential of the current-free field \mathbf{B}_p with the choice of the gauge $\mathbf{V} \cdot \mathbf{A}_p = 0$. Note that the current-free field \mathbf{B}_p is fully specified by the distribution of the vertical component of magnetic field B_z on the surface S . Since the current sustaining \mathbf{B}_p is confined to the surface, the vertical component of the current on the surface is zero, and it follows $A_{pz} = 0$ on the surface. If either magnetic field or mass motion is confined to a finite area of the surface S_p , the integral is fully determined observationally given a time series of line-of-sight magnetograms of the surface S_p . Here the vertical component of magnetic field B_z is obtained from line-of-sight magnetograph observations after correcting for geometrical effects. The horizontal components of velocity \mathbf{v} are determined using the technique of LCT as already described in this section. The term \mathbf{A}_p can be computed based on the observed B_z .

Using the Fourier transform method is an efficient way to calculate \mathbf{A}_p . In Cartesian coordinates, the equations for A_{px} and A_{py} reduce to

$$\frac{\partial^2 A_{px}}{\partial x^2} + \frac{\partial^2 A_{px}}{\partial y^2} = -\frac{\partial B_z}{\partial y}, \quad (3)$$

$$\frac{\partial^2 A_{py}}{\partial x^2} + \frac{\partial^2 A_{py}}{\partial y^2} = \frac{\partial B_z}{\partial x}, \quad (4)$$

and their Fourier solutions are given by

$$A_{px} = FT^{-1} \left[\frac{jk_y}{k_x^2 + k_y^2} FT(B_z) \right], \quad (5)$$

$$A_{py} = FT^{-1} \left[-\frac{jk_x}{k_x^2 + k_y^2} FT(B_z) \right] \quad (6)$$

when the Fourier transform of a function $A(x, y)$ is defined by

$$FT(A) = \sum_{x,y} A(x, y) \exp(-jk_x x - jk_y y) \quad (7)$$

with $j \equiv \sqrt{-1}$. We perform the Fourier transforms over the whole field of view $270'' \times 270''$ to determine the vector potential at every pixel point inside the field of view. But the helicity change rate integration of equation (2) is done over the finite region of interest that is smaller than the field of view.

Our approach for determining the rate of magnetic helicity change is somewhat different from previous ones. Wang (1996), for example, estimated the magnetic helicity of an active region based on the force-free assumption and related the change rate of the force-free α to the rate of magnetic helicity change. In the present study, however, we do not make any assumption on the magnetic field. Moreover, we determine both of the fields \mathbf{v} and B_z at every instant from observations. This is contrasted to previous studies that assumed a stationary velocity field—like solar differential rotation—and computed the B_z field as a function of time (e.g., DeVore 2000).

The observational determination of dH/dt is subject to errors since the observed quantities \mathbf{v} and B_z are not free from errors. The geometric projection produces errors not only in the observed B_z but also in \mathbf{v} . Fake flux elements and their fake motion in regions of strong horizontal fields are extreme examples of these errors. But as we shall see, these regions are very localized, so their contribution to dH/dt appears insignificant. The other source of the errors in dH/dt may be poor spatial resolution. Note that A_p is very insensitive to spatial resolution, since it is an integrated quantity of B_z and is a smoothly varying function of position. The spatial resolution does not affect the measurement of the magnetic flux $B_z dS$ either. The most sensitive to spatial resolution is the measurement of \mathbf{v} . The velocity of a small magnetic element may be underestimated in poor spatial resolution observations. Moreover, the velocity may have a bigger uncertainty in poor spatial resolution observations since the features are smeared.

3. RESULTS

3.1. Filament Formation

Figure 1 shows the H α images of the active region NOAA 8668 taken at BBSO over the several observing days when a filament was under formation. During the first two days, the

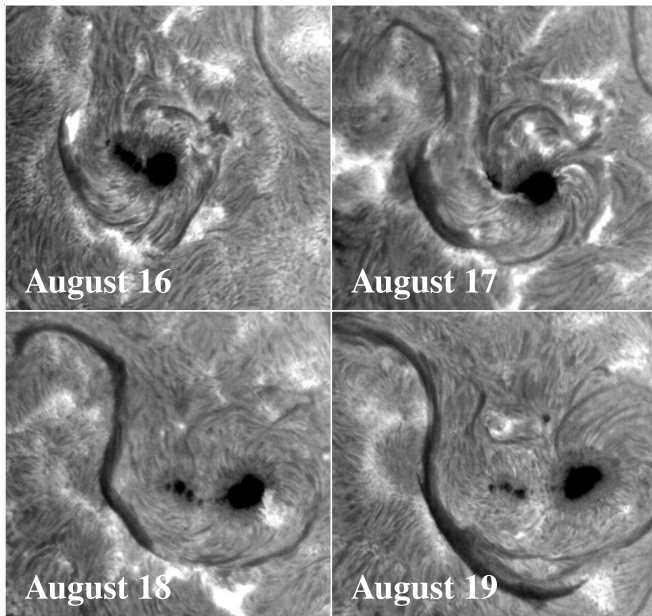


FIG. 1.— $H\alpha$ center-line images of the active region NOAA 8668 that show a reverse S-shaped filament under formation.

southern part of the filament evolved from highly sheared $H\alpha$ loops that constitute a counterclockwise whorl into the sunspots of leading (positive) polarity. The northern part emerged from the channel of $H\alpha$ fibrils that delineated a polarity reversal boundary. Later, the two parts linked to each other, and as a result, the filament became of a reverse S-shape when it fully developed.

The $H\alpha$ image taken on August 16 exhibits a bright $H\alpha$ patch at the junction of the two parts. This emission patch was associated with a big canceling magnetic feature and hence appears to be a result of magnetic reconnection that may have resulted in the linkage of the northern and southern parts. The magnetic flux change in this canceling magnetic feature will be examined in detail in the following.

This filament was previously studied by Chae et al. (2000). They obtained chromospheric transverse velocity fields of this active region from high-cadence $H\alpha$ 0.6 Å observations performed on 1999 August 17. A series of chromospheric upflow events were identified in association with a small canceling magnetic feature near the southern part of the filament. This finding supports the picture that cool plasma is injected to the filament by reconnection in the low atmosphere.

The filament has dextral chirality—namely, the axial magnetic field of the filament is directed rightward to an observer facing the polarity reversal boundary from the positive flux side. Chae (2000) used EUV data taken by *TRACE* and demonstrated that this filament has negative magnetic helicity

3.2. Magnetic Flux Evolution

Figure 2 shows the evolution of flux distribution in the active region between 1999 August 16 and 18. The active region consists of several leading sunspots of positive polarity and the trailing plage of negative polarity. The filament of interest was formed over the polarity reversal boundary between them. We define the area surrounding the polarity reversal boundary N as the neighborhood of

the filament. It is expected that most of the field lines passing through the filament are rooted somewhere inside N and hence the evolution of photospheric magnetic fields inside N directly affects the evolution of the filament.

3.2.1. Flux Changes in the Filament Neighborhood

Figure 3 shows positive magnetic flux and negative magnetic flux integrated over the filament neighborhood N as functions of time. We find from this figure that there exists flux imbalance, the positive flux ($F_+ = 1.4 \times 10^{22}$ Mx) being bigger than the negative flux ($F_- = -1.1 \times 10^{22}$ Mx). This flux imbalance may be because the field lines starting from the umbra of the sunspot do not return to the solar surface inside N. In fact, the positive flux of the sunspot umbra alone is close to the unbalanced flux. We also find from the figure that both the positive flux and negative flux decreased throughout the 3 days. The amounts of flux decrease are $\Delta|F_+| = -3.3 \times 10^{21}$ Mx (24%) for the positive polarity and $\Delta|F_-| = -4.6 \times 10^{21}$ Mx (42%) for the negative polarity. These values are rather high and need to be explained.

We first examine the systematic contribution of the projection error correction to the observed flux changes. As shown in Appendix A, a fake change of magnetic flux due to the projection correction error may be manifest in the change of the net flux, which is given by $\Delta F_N = \Delta|F_+| - \Delta|F_-| = 1.3 \times 10^{21}$ Mx. This observed increase of the net flux implies $B_x < 0$. This is consistent with the fact that the polarity inversion line lies between the western sunspot area of positive polarity and the eastern plage area of negative polarity. The horizontal magnetic fields around the polarity inversion line with such polarity orientation are expected to be predominantly directed to the west ($B_x < 0$). At far off-disk-center regions with $B_x < 0$ and $|B_x| \geq |B_z|$, fake flux elements of negative polarity may appear. The negative flux patch 1 shown in Figure 2 is obviously such a fake flux element, since the region is at the outer edge of a sunspot penumbra where the horizontal magnetic field is stronger than the vertical field. Therefore, we may regard the ratio $\Delta F_N/|F_-| \approx 0.12 = 12\%$ as a rough estimate of the relative error of the negative magnetic flux measurement introduced by the simple geometric correction that has neglected horizontal magnetic fields. Note, however, that this estimate is smaller than the other 30% change of $|F_-|$, so the projection correction error alone cannot explain all of $\Delta|F_+|$ and $\Delta|F_-|$. Our result is in fact consistent with the past reports that the average rate of flux removal from active regions is about $10\% \text{ day}^{-1}$ (Howard & Labonte 1981; Wallenhorst & Topka 1982).

A careful comparison of August 16 and 18 magnetograms presented in Figure 2 reveals that noticeable loss of magnetic flux occurred in the region CMF and in the patches in the ringlike area surrounding the sunspots of positive polarity. These patches are of mixed polarity and move outward, so they may be identified with moving magnetic features (MMFs; Harvey & Harvey 1973). They eventually disappear or merge with the plage or network. The physical nature of MMFs is not understood so far, and so we do not know whether or not the disappearance of MMF flux is the same process as the flux loss as seen in CMF.

3.2.2. Flux Change in the Canceling Magnetic Feature

Figure 3 also shows the positive flux of the CMF as a function of time. We find that the temporal variation of the

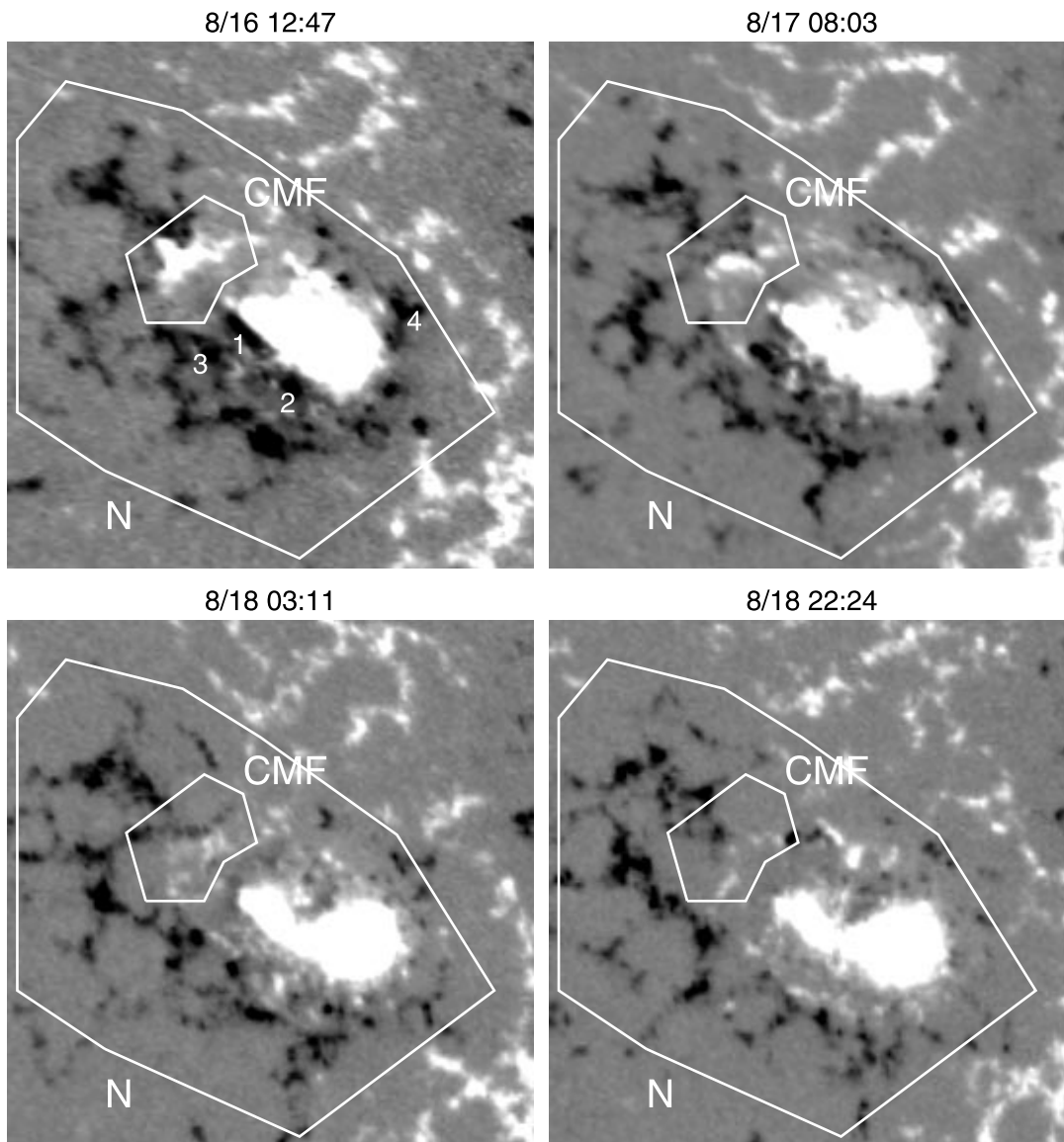


FIG. 2.—*SOHO/MDI* magnetograms showing the time variation of the flux distribution in the active region. The polygon N represents the neighboring region of the polarity reversal boundary over which the filament was formed. The smaller polygon CMF indicates the region of the dominant canceling magnetic feature. The field of view is $270' \times 270'$.

flux is fairly described by an exponential function

$$F = F_0 \exp [-(t - t_0)/\tau] \quad (8)$$

after the instant $t_0 = \text{August } 16 \text{ } 08:00 \text{ UT}$ with the values of $F_0 = 1.4 \times 10^{21} \text{ Mx}$ and $\tau = 28 \text{ hr}$. This result on the time variation of flux in the CMF is qualitatively consistent with the previous result on the flux change of a canceling magnetic feature obtained by Chae et al. (2000). They studied a much smaller canceling magnetic feature and obtained the parameters $F_0 = 1.2 \times 10^{19} \text{ Mx}$ and $\tau = 0.67 \text{ hr}$. Note that the bigger canceling magnetic feature has a longer e -folding time than the smaller one. This comparison suggests that the exponential behavior of flux decrease may be a universal characteristic of canceling magnetic features irrespective of size, and big canceling magnetic features may consist of a time series of many smaller canceling magnetic features.

There may be a worry that the flux decrease might be due to the error in projection correction since the cancellation

occurred at the polarity inversion line where horizontal magnetic fields might be strong. However, the existence of the positive flux element and its flux decrease cannot be explained by the projection error. Suppose strong horizontal magnetic fields exist near the polarity inversion line inside the CMF. Then, it would be expected from the flux configuration that the horizontal fields are directed to the east; i.e., $B_x < 0$. This means that $\epsilon(B_z) < 0$, $(\Delta F)_\epsilon > 0$ (see Appendix A), contradicting our finding of the existence of the positive flux elements and their flux decrease with time. Moreover, if flux cancellation is a result of magnetic reconnection in the low atmosphere as often proposed (e.g., Litvinenko 1999), it is likely that magnetic fields are predominantly vertical at the interface of flux cancellation since flux cancellation is a result of the collision and reconnection of initially vertical field lines of opposite polarity. Reconnection produces new field lines with strong horizontal fields, but their contribution to the flux measurement

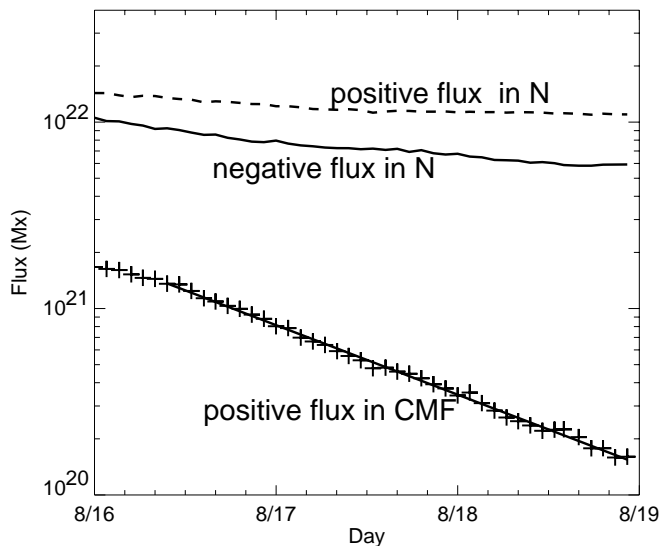


FIG. 3.—Time variations of the positive flux inside the polygon CMF and the positive and negative fluxes inside the filament neighborhood N. The amounts of flux decrease are 1.5×10^{21} , 3.3×10^{21} , and 4.6×10^{21} Mx, respectively. The solid line is an exponential fit of the CMF flux variation with an e -folding time of 28 hr.

may still be small since the spatial extent of the reconnection area is very small and the reconnected field lines submerge and disappear very soon after they are created. Therefore, we think that the projection correction error is not significant in our measurement of the flux change in CMF.

If flux cancellation is really a result of magnetic reconnection, thermal energy and kinetic energy should be released at the location. The August 16 H α image of Figure 1 shows an emission patch at the flux-canceling region CMF. In addition, from August 16 to 18, we have found a series of small-scale transient brightenings and jets in CMF from EUV data taken by *TRACE* (J. Chae, Y. Moon, H. Wang, & P. Goode 2001, in preparation). These findings support the reconnection picture of flux cancellation.

3.3. Photospheric Motion

Figure 4 shows the transverse velocity map of the active region at a specific time, with the solar differential rotation not being included. The rms speed of magnetic concentrations is about 0.20 km s^{-1} . This value is bigger than 0.07 km s^{-1} , the rms speed of solar differential rotation in the same area.

3.3.1. Radially Expanding Motion

In addition to random motion, several kinds of organized motion persisted over the observing days. Most prominent was a radially expanding motion of the leading sunspots and the surrounding magnetic concentrations of trailing polarity that has its origin at the center of the main sunspot. The expansion has a peak speed of about 0.5 km s^{-1} at the penumbra of the main sunspot. This expansion is associated with MMFs. It has been known that MMFs move at a speed of a few tenths to over 2 km s^{-1} , with an average of about 1 km s^{-1} (Harvey & Harvey 1973). Thus, the speeds we obtained appear to be consistent with but smaller than the known values of MMFs, possibly because of the smearing effect introduced by using $\text{FWHM} = 8''$ for LCT, which is much bigger than the size of MMFs ($\leq 2''$).

3.3.2. Shear Motion

Another organized motion is the shear motion near the polarity reversal boundary. This pattern is less obvious than the radial motion, because it is confined to a narrow stripe along the polarity reversal boundary and is contaminated with random motion. Nevertheless, a careful examination of the velocity maps can reveal several magnetic concentrations that move significantly in parallel with the polarity reversal boundary (note the circles in Fig. 4). We find that the negative magnetic concentrations of negative polarity move clockwise with respect to the center of the main sunspot, whereas the sunspots of positive polarity rotate in the opposite direction. The speed of shear motion ranges from 0.2 to 0.5 km s^{-1} , which is comparable to that of the radial expansion.

Motion near the polarity reversal boundary might be a little contaminated by the errors in projection correction when combined with solar rotation. Particularly, fake flux elements that appear at regions of strong horizontal magnetic fields may display fake motion in the east direction. The transverse motion at region 1 in Figure 4 may be an example of such fake motion. The measured speed is comparable to the one that is theoretically estimated in Appendix B. To the contrary, the strong shear flows at regions 2 and 3 may be real. We have examined a movie of magnetograms and found that the flux concentrations really moved in the direction deduced by LCT. The strong flux concentrations at the regions are well separated from the sunspots, and hence their magnetic fields may be more vertical than horizontal. And even if magnetic fields in filaments are known to be mostly horizontal, their footpoints are expected to be vertically rooted in the photosphere because of magnetic buoyancy (see, e.g., Zwaan 1987). Thus, the shear flow at the regions may be little contaminated by fake motion due to the projection of horizontal field components.

The shear motion feeds magnetic helicity into the corona, the sign of which is determined by the integral of $\mathbf{v} \cdot (-2B_z \mathbf{A}_p)$. The distribution of $-\text{sgn}(B_z) \mathbf{A}_p$, as shown in Figure 5, has a counterclockwise rotational pattern around the center of the positive sunspot in the sunspots of positive polarity and a clockwise rotational pattern around the same point in the negative polarity magnetic concentrations, both of which are opposite to the observed shear flow directions. Therefore, the shear motion feeds negative magnetic helicity into the corona. Note that this sign is the same as that of the magnetic helicity of the filament.

3.3.3. Converging Motion

Finally, converging flow was seen in the northern portion of the polarity reversal boundary where the dominant flux cancellation occurred. Figure 6 shows the enlarged view of the transverse velocity maps of the flux-canceling region. The cancellation of magnetic flux may be due to the collision of positive flux and negative flux that is driven by the persistent westward migration of magnetic concentrations of negative polarity. This westward migration may be another manifestation of the clockwise rotation of negative flux concentrations around the center of the leading sunspots that is also manifest in the shear flow pattern mentioned above. The speed of the migration is up to 0.3 km s^{-1} . Magnetic concentrations of positive polarity, however, do not display any persistent flow pattern and move more or less randomly. As a result, not only the negative mag-

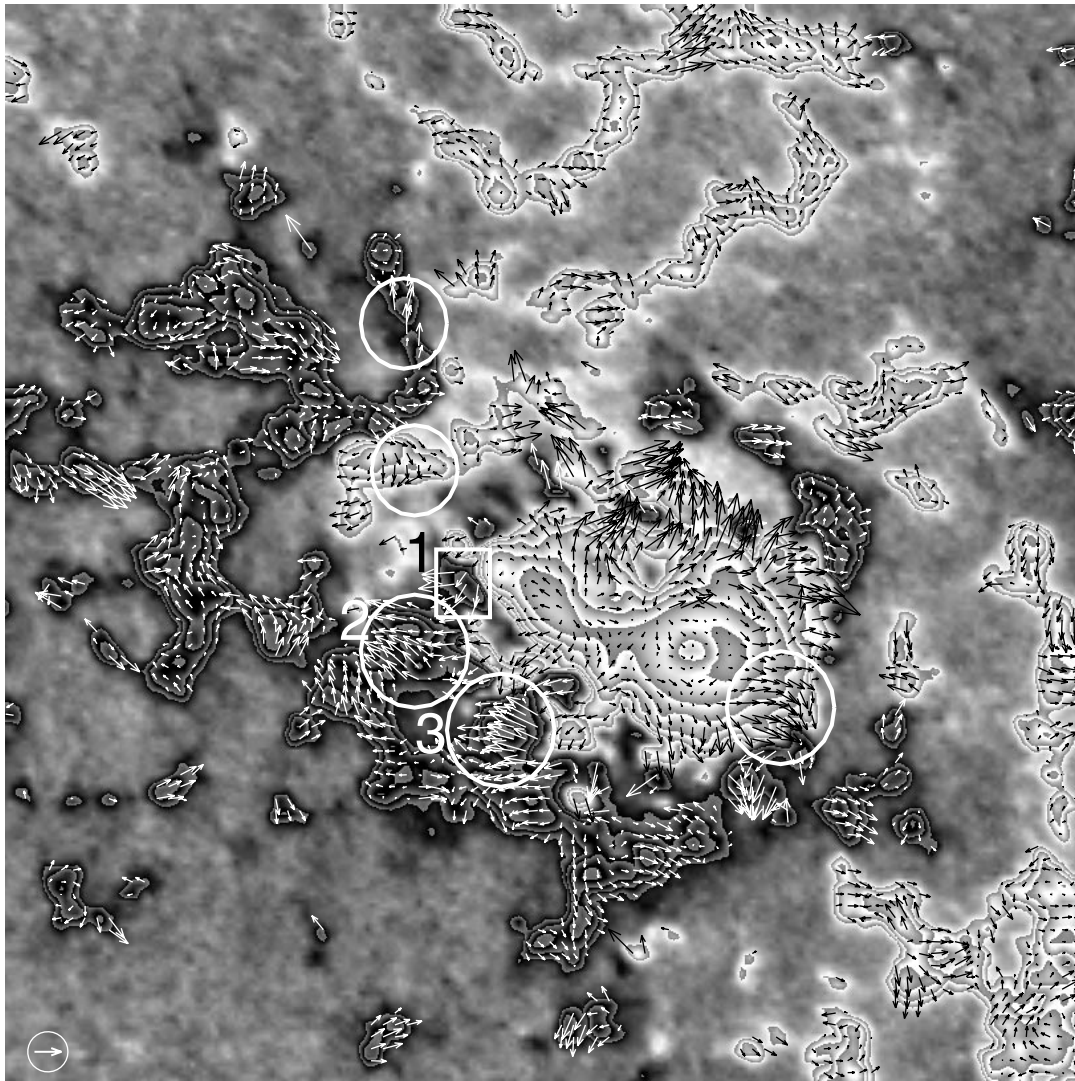


FIG. 4.—Vector field v map of the active region at a specific time superposed on the gray-scale flux density map. The arrow enclosed by the circle at the lower left corner measures a speed of 0.3 km s^{-1} . Regions with dominant shearing flows are enclosed by the circles. Gray-scale discontinuities represent the flux density levels of $\pm 50, 100,$ and 200 G and so on.

netic concentrations but also the polarity reversal boundary moves westward.

Several small polarity reversal interfaces with very steep flux density gradient are seen in Figure 6. These are the specific places where flux cancellation occurs. The relative speeds between positive and negative magnetic concentrations at the interfaces are about 0.1 km s^{-1} or smaller, which is significantly smaller than the speed of the organized westward migration. This discrepancy may be due to internal dynamics of flux cancellation such as the increase of magnetic pressure by the pile-up.

3.4. Magnetic Helicity Changes

3.4.1. Spatial Distribution of Local Contribution

The gray-scale map in Figure 7 represents the distribution of $G \equiv v \cdot (-2B_z A_p)$ in the filament neighborhood, which can be interpreted to be the local contribution of photospheric motion to the change rate of magnetic helicity in the coronal volume. The imposed arrows indicate transverse velocities. Local maxima of $|G|$ exist in association with large $|v|$, as expected. The sign of G is related to the

direction of transverse motion. It is predominantly negative in the negative flux side that shows clockwise rotation of the magnetic concentrations and in the southern part of the positive sunspot that shows counterclockwise rotation. Positive values of G appear in the northern part of the positive sunspot because of the weak clockwise rotation pattern seen in this part. Note that the magnitude of G is bigger in the sunspot area than in the plage area since both B_z and A_p have large magnitude in the sunspot area. However, because of its mixed polarity character of G , the net contribution of the sunspot is comparable to or less than that of the plage area. At this specific instant, the integration of G over N is found to be $-4.0 \times 10^{40} \text{ Mx}^2 \text{ hr}^{-1}$.

3.4.2. Temporal Variation

Figure 8a shows the temporal variation of dH/dt due to photospheric motion over the observing period without differential rotation taken into account. We find that dH/dt exhibited large-amplitude fluctuation over time. So we have plotted in the figure the average rates for the time bins of 3 hr together with the error bars that are equal to the stan-

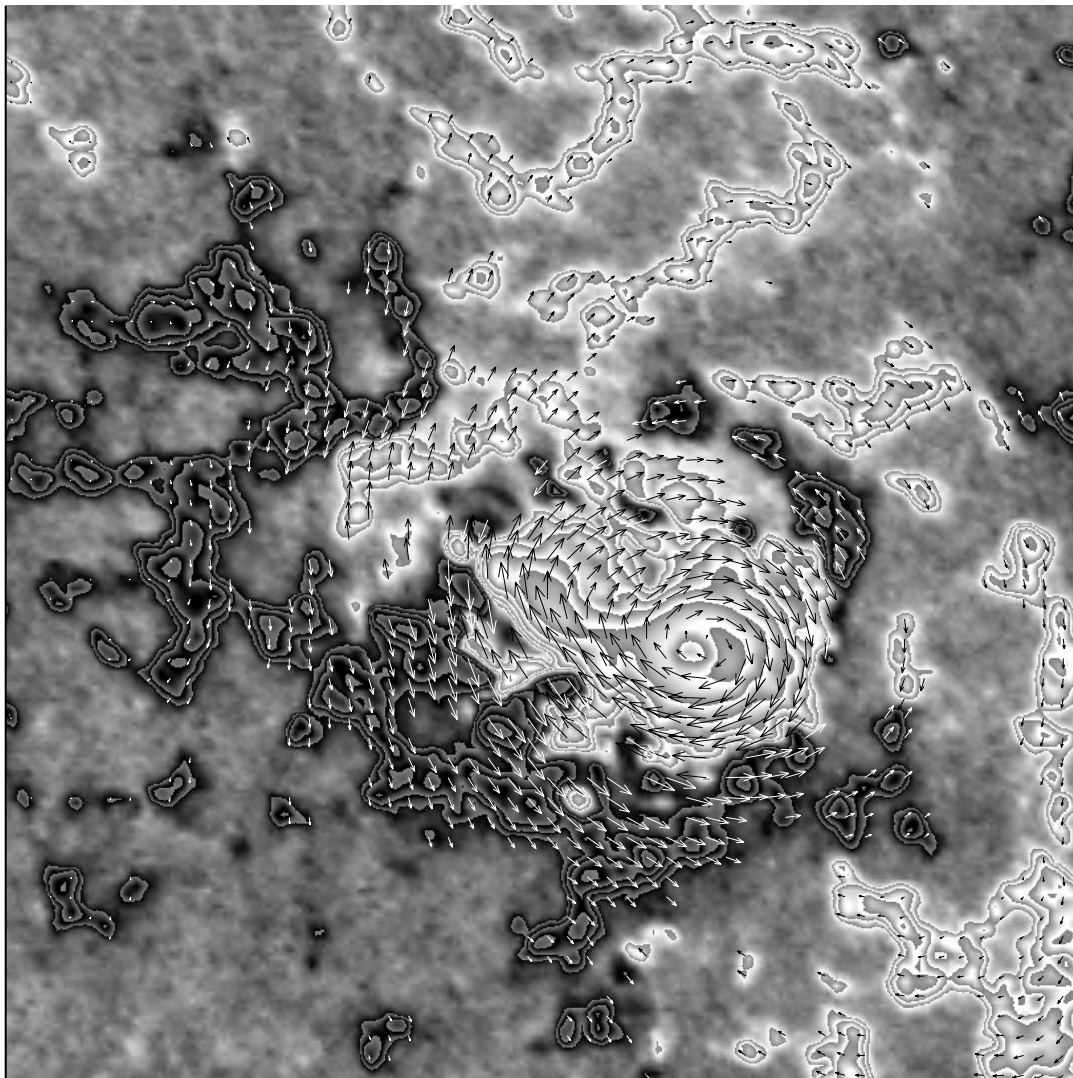


FIG. 5.—Vector field $-\text{sgn}(B_z)A_p$ map of the active region superposed on the gray-scale flux density map

standard deviation. It is obvious from this figure that the helicity injection rate remained predominantly negative throughout the observing period. The mean helicity injection rate was found to be $\langle dH/dt \rangle = -5.8 \times 10^{40} \text{ Mx}^2 \text{ hr}^{-1}$. The magnetic helicity change that took place during the observing period of 50 hr is then $\Delta H \approx 50 \langle dH/dt \rangle = -2.9 \times 10^{42} \text{ Mx}^2$. In fact, the figure shows that the absolute value of helicity injection rate significantly decreased on August 18 and the helicity injection mainly occurred on August 16 and 17, during which days the filament formation proceeded. This temporal characteristic implies that the helicity injection may have been physically related to the formation of the filament.

The fluctuating component of the variation of helicity injection rate seen in Figure 8 has a standard deviation comparable to the mean component. We have found that the fluctuating timescale is down to 10 minutes. We think that the fluctuations mostly represent random errors in velocity measurements, especially inside the sunspot. Flux distribution inside the sunspot is more or less continuous in low-resolution magnetograms, which inhibits precise determination of velocity inside the sunspot. In addition, small errors in velocity determination inside the sunspot are

amplified in helicity injection rate determination because magnetic field and vector potential are strong inside the sunspot. This may explain why the fluctuation amplitude is comparable to the signal itself.

3.4.3. Contribution by Differential Rotation

Figure 8b shows the temporal variation of dH/dt due to solar differential rotation only, during the same period. The average rate of helicity change due to differential rotation is about $-0.9 \times 10^{40} \text{ Mx}^2 \text{ hr}^{-1}$. This value is very close to the one predicted by DeVore (2000), $(dH/dt)_D = (\pi/32)\Omega F^2 = -1.0 \times 10^{40} \text{ Mx}^2 \text{ hr}^{-1}$, with the use of $\Omega \equiv dv_{\text{rot}}/(R_{\odot} db) = -3 \times 10^{-7} \text{ s}^{-1}$ and $F = 1.0 \times 10^{22} \text{ Mx}$. It is an order of magnitude smaller than the contribution by the other shear flow. Therefore, during our observing run, the solar differential rotation is less important in the change of magnetic helicity than the observed shear flow pattern. This is not surprising since the rms speed of the differential rotation was shown to be much smaller than that of observed transverse motion. The effect of the differential rotation, however, increased with time because of the increase of the latitudinal extent of the active region, and the absolute value of dH/dt reached $1.5 \times 10^{40} \text{ Mx}^2 \text{ hr}^{-1}$

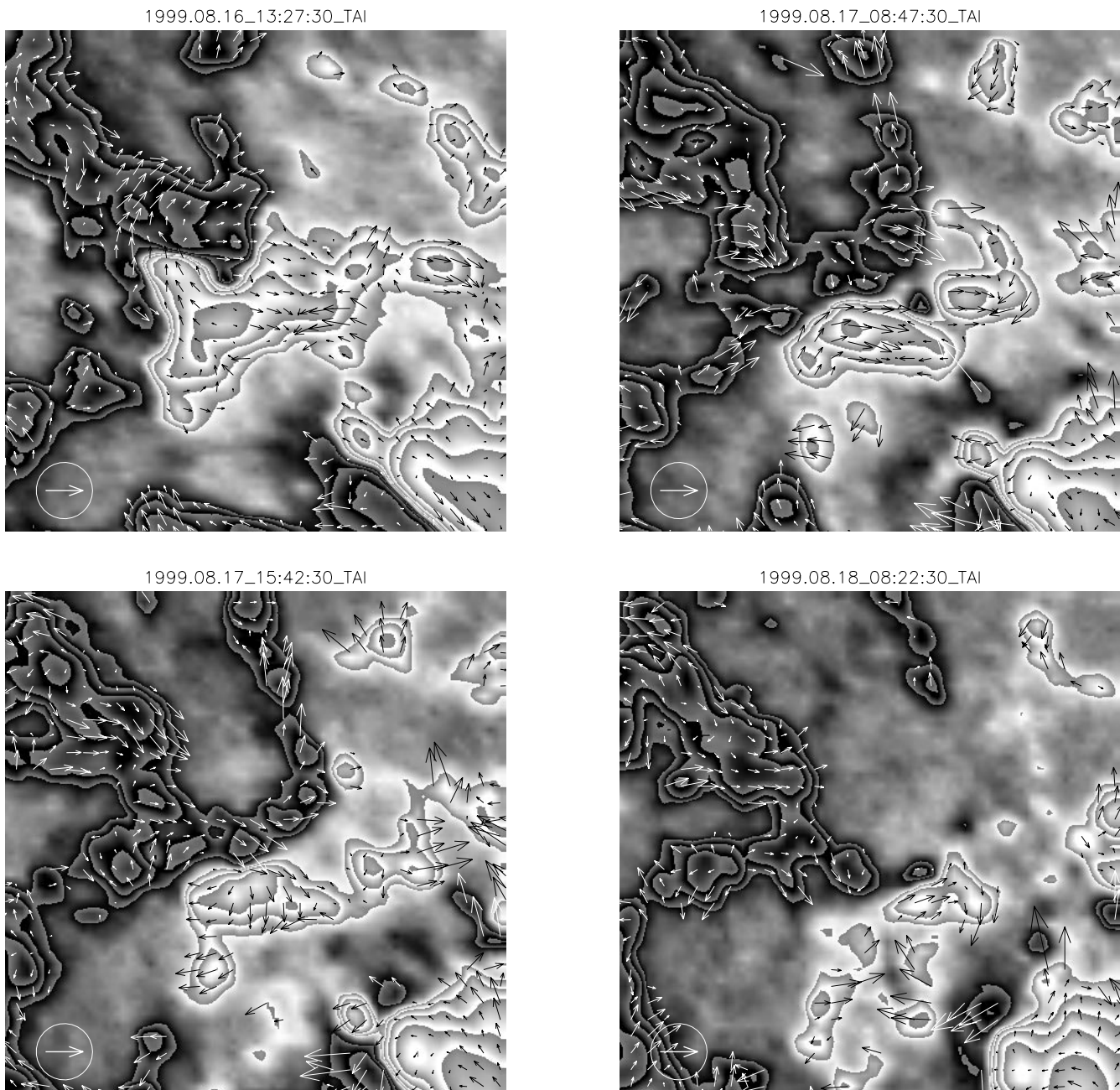


FIG. 6.—Transverse velocity vector maps of the flux-canceling region at four different times. The arrow inside the circle measures a speed of 0.3 km s^{-1} .

on August 18. This time variation is contrasted with the other kind of shear motion, the effect of which decreased with time. Thus, the differential rotation may have been important in the change of magnetic helicity on the days later than August 18.

4. DISCUSSION

4.1. Magnetic Evolution Associated with Filament Formation

From an analysis of *SOHO*/MDI magnetograph observations of NOAA 8668, we have investigated the evolution of magnetic fields seen in the photosphere during the formation of a reverse S-shaped filament and have obtained several observational results supporting that the formation of the filament is strongly associated with photospheric magnetic evolution.

First, we found that the total magnetic flux in the neighborhood of the filament decreased with time. The flux decrease may be due to flux cancellation, the collision and subsequent mutual loss of positive flux and negative flux, which occurred ubiquitously along the polarity reversal boundary. Particularly, a large canceling magnetic feature was found to be well correlated with the filament under formation both spatially and temporarily. This result confirms previous studies as reviewed by Martin (1998).

We also found that the footpoints of magnetic field lines were subject to different kinds of organized motion. Most of all, we have discovered a pattern of shearing motion near the polarity reversal boundary above which the filament formation proceeded, by applying the technique of local cross-correlation tracking to the magnetograms taken by *SOHO*/MDI. Shear motion has been frequently introduced

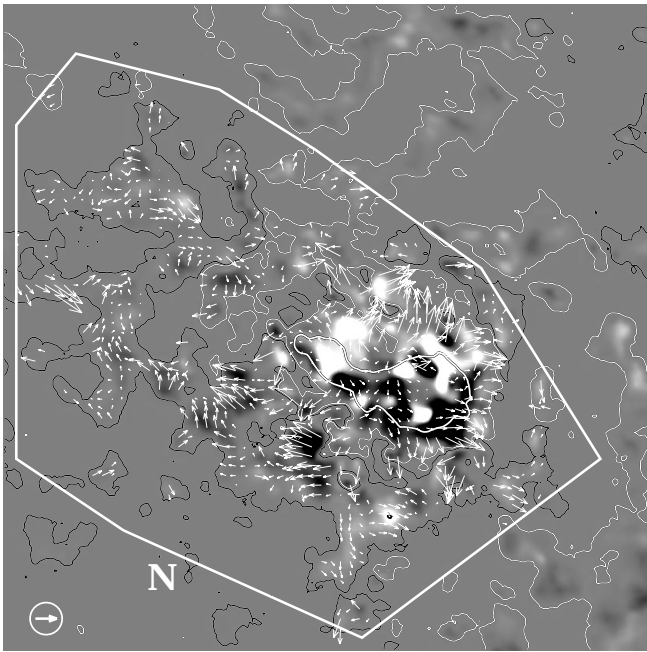


FIG. 7.—Gray-scale map of $-2(v \cdot A_p)B_z$ and the superposed transverse velocity vectors. The contours are the flux density levels of ± 20 and 400 G.

as inputs to theoretical models of filament formation (e.g., Choe & Lee 1992; DeVore & Antiochos 2000) but has hardly been reported from observations, possibly because of the very limited availability of high-quality magnetogram data with a good time resolution that can be used to determine horizontal velocities in filament-forming regions. High-quality line-of-sight magnetograms taken at BBSO were exploited to determine the horizontal velocities of intranetwork and network magnetic fields in the quiet Sun (Wang et al. 1996) but have not been used to determine the horizontal velocities in filament-forming regions. Our results demonstrate that the vast amount of magnetogram data taken by *SOHO*/MDI—when combined with the technique of local correlation—provides unprecedented opportunities for the investigation of the photospheric

motion of magnetic field line footpoints at various regions at different evolutionary stages.

The shear motion that we identified has a pattern of counterclockwise rotation around the center of the sunspots in the positive (leading) polarity region. As a consequence, the shear motion fed negative magnetic helicity, which is of the same sign as the magnetic helicity of the filament that has dextral chirality. Moreover, the effect of the shear motion was stronger during the earlier days when the formation actively proceeded than during the latter days when the filament was fully formed. These characteristics strongly support that the formation of the filament was physically related to the shear motion.

In addition, we identified converging motion of magnetic concentrations toward the polarity reversal boundary. The converging motion appears to be another manifestation of the clockwise rotation of the magnetic concentrations around the center of the biggest leading sunspot. As a consequence, negative magnetic concentrations collided with positive ones, and flux cancellation occurred in the northern part of the filament.

We have determined two important physical parameters of magnetic evolution: the amount of magnetic flux lost by cancellation in the main canceling magnetic feature ($\Delta F = 1.5 \times 10^{21}$ Mx) and the amount of magnetic helicity change due to the photospheric shuffling motion of field-line footpoints [$\Delta H = (-2.9 \pm 3.0) \times 10^{42}$ Mx²]. These two values allow us to examine the relationship between the observed magnetic evolution and the filament formation quantitatively.

4.2. Canceled Magnetic Flux

When magnetic reconnection occurs in the low atmosphere, two sets of field lines are newly made. One is a set of field lines near the surface, and the other is a set of field lines high above the surface. The low-lying field lines may have large curvatures and hence can submerge below the photosphere by the force of magnetic tension. Flux cancellation is usually interpreted as the submergence of such field lines (e.g., van Ballegoijen & Martens 1989). A consequence of this interpretation is that the flux of the field lines newly made high above the surface should be equal to the canceled magnetic flux. Suppose the upper lying field lines form

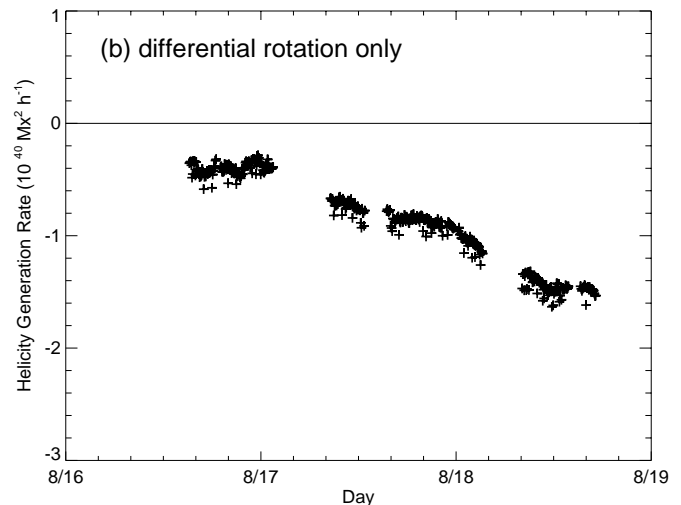
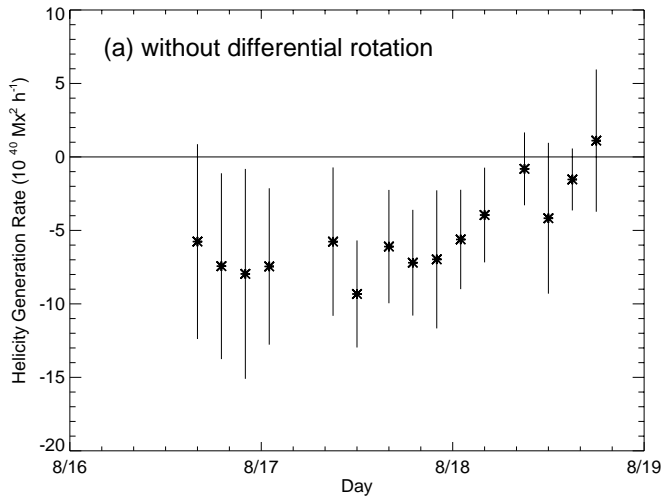


FIG. 8.—Time variations of the rates of magnetic helicity change (a) by photospheric motion other than differential rotation and (b) by differential rotation only.

a filament as is theoretically proposed (Priest, van Ballegoijen, & Mackay 1996; Litvinenko & Martin 1999). Then the magnetic flux of a filament is expected to be the same as the canceled flux, and it would be interesting to compare the observed canceled flux with an estimated flux of the filament.

The magnetic flux of the filament may be estimated from the equation $F_F = B_F A$, where B_F is the axial field strength of the filament and A is its cross section. According to the Zeeman measurements done by Kim & Alexeyeva (1994), the line-of-sight components of active region prominence magnetic fields range from 0 to 60 G, and their average value is about 22 G. If it is assumed that prominence magnetic fields are predominantly along the axial direction and the inclinations of prominence axes to the line of sight are random, then the filament field strength B_F is less than 100 G and is most likely to be 35 G. For a conservative (i.e., biggest) estimate, we choose $B_F = 100$ G.

Next, we assume that the cross section is a circle with a diameter that is equal to the observed width $w = 8000$ km. Then, the cross-sectional area is equal to $\pi w^2/4$, and we get an estimate $F_F = 5.0 \times 10^{19}$ Mx. This value is much smaller than the observed canceled flux $\Delta F = 1.5 \times 10^{21}$ Mx. The big discrepancy between the observed canceled flux and the estimated filament flux is hardly explained by any uncertainty in estimating F_F . A possible explanation is that only a small fraction of the upper lying field lines created by magnetic reconnection pass through the filament. In other words, magnetic reconnection may have created a new magnetic structure that is much bigger than the newly formed filament.

What would be the nature of the new magnetic structure and its relation to the newly formed filament? A plausible structure may be a flux rope (twisted flux tube) inside which the filament is embedded (Priest, Hood, & Anzer 1989). According to this picture, the cross section of the flux rope is πa^2 , with the radius a being bigger than the observed width w . If we choose $a = 2w$, then the axial magnetic flux of the rope is $F_{FR} = 8.0 \times 10^{20}$ Mx, which is 16 times F_F . This value is of the same order of magnitude as but is still smaller than the canceled flux ΔF .

This discrepancy between the axial flux of the flux rope and the canceled flux ΔF may have physical significance. First, we may have to consider the possibility that initially colliding loops are close to a potential configuration. In this case, the magnetic fields have a significant amount of components perpendicular to the polarity inversion line, and as a result of the reconnection, only a fraction of the canceled flux would be converted to the axial flux of the flux rope. But this is not the case. As seen from Figure 1, the fibrils around the filament under formation are well aligned in parallel with the filament itself, which indicates that the magnetic fields are predominantly along the polarity inversion line, being far from the potential configuration. This is a well-known necessary condition for filament formation (Martin 1998).

A possible explanation may be that an additional structure is created by the reconnection, as represented by the flux cancellation. We conjecture that it may be a coronal arcade that overlies the flux rope. The comparison made above suggests that the axial flux of the arcade should be comparable to or bigger than that of the flux rope, implying that the coronal arcade may be highly sheared. Note that both the flux rope and the coronal arcade is considered to

be of the same origin, magnetic reconnection. This view is slightly different from the conventional theoretical studies that regard the filament formation as a result of flux transport from the coronal arcade to the flux rope. Further studies are required to support or disprove the possibility of the same origin of the coronal arcade and the filament.

4.3. Magnetic Helicity Change

Since a filament is a highly nonpotential magnetic structure that has a significant amount of magnetic helicity, the formation of a filament requires the supply of magnetic helicity as well as mass and magnetic flux. It may be said that the magnetic helicity of a filament was originally contained in the initial magnetic structures such as fibrils or sheared loops. In this case, one needs to explain further the origin of magnetic helicity in the initial magnetic structures and the way of transporting helicity from the initial structures to the filament. Suppose that photospheric shear motion injected magnetic helicity into the magnetic structures around the polarity inversion line and some of this injected magnetic helicity was supplied to the newly formed filament or, more plausibly, a flux rope inside which the filament was embedded. Then, the amount of injected magnetic helicity is expected to be comparable to or larger than the magnetic helicity of the flux rope.

We have already found the magnetic helicity injected by the photospheric shear motion is about $\Delta H = -2.9 \times 10^{42}$ Mx². Now let us estimate the magnetic helicity of the flux rope H_{FR} to test the above hypothesis. Its magnetic helicity is given by $H_{FR} = nF_{FR}^2$, where n is the number of turns from one footpoint to the other. Chae (2000) showed that the filament is dextral and has negative helicity. Thus, n should be negative, being consistent with the sign of the observed ΔH . Moreover, Figure 1 of Chae (2000) suggests that $n \simeq -1$. Therefore, the magnitude of H_{FR} mostly depends on F_{FR} . The use of $F_{FR} = 8 \times 10^{20}$ Mx yields an estimate of $H_{FR} = -0.64 \times 10^{42}$ Mx², a value smaller than $\Delta H = -2.9 \times 10^{42}$ Mx². This means that the magnetic helicity injected by the photospheric shear motion is likely to be more than enough for the flux rope, not to speak of the filament itself.

It is also interesting to compare ΔH with the magnetic helicity of all the field lines created by the reconnection. The same choice of $n = -1$ and the use of the observed canceled flux $\Delta F = 1.5 \times 10^{21}$ Mx leads to $H_{new} = -(\Delta F)^2 = -2.3 \times 10^{42}$ Mx². This value is comparable to the measured $\Delta H = -2.9 \times 10^{42}$ Mx². This coincidence may have physical significance. Even if the flux cancellation is a localized phenomenon, it may be involved with a large-scale restructuring of magnetic fields in the active region, which is likely to be the creation of the flux rope and its overlying sheared arcade. Meanwhile, the photospheric shear motion applied to the field-line footpoints of the newly created magnetic system may have supplied magnetic helicity to the structure that may be enough for keeping it highly nonpotential. Very interestingly, the observed magnetic flux $\Delta F = 1.5 \times 10^{21}$ Mx and the estimated magnetic helicity $|H_{new}| = 2.3 \times 10^{42}$ Mx² are of the same orders of magnitude as the magnetic flux $F_{imc} = 1 \times 10^{21}$ Mx and the magnetic helicity $|H_{imc}| = 2 \times 10^{42}$ Mx² that were obtained for a typical interplanetary magnetic cloud by DeVore (2000). This new magnetic system would be identified as an interplanetary magnetic cloud, after it erupts and escapes to interplanetary space.

TABLE 1
OBSERVED OR ESTIMATED MAGNETIC FLUXES AND MAGNETIC HELICITIES OF
DIFFERENT MAGNETIC STRUCTURES IN THE ACTIVE REGION

Structure	Magnetic Flux ($\times 10^{21}$ Mx)	Magnetic Helicity ($\times 10^{42}$ Mx ²)
Active region negative flux	10	
Active region negative flux decrease	4.6	
Positive flux decrease in CMF	1.5	
Shear motion		2.9
Differential rotation		0.5
Filament (visible part in H α)	0.05	
Flux rope enclosing filament	0.8	0.64
New structure (flux rope + coronal arcade?).....	1.5	2.3
Typical interplanetary magnetic cloud	1	2

Finally, observed or estimated magnetic fluxes and magnetic helicities of different magnetic structures in the active region are summarized in Table 1.

5. CONCLUSION

We have presented results showing that the formation of a filament in the active region NOAA8668 is strongly associated with magnetic evolution observed in the photosphere. Evidence includes the existence of a shear motion, the convergence of magnetic concentrations toward the polarity reversal boundary, and the cancellation of magnetic flux. The shear motion and the converging motion seem to have a common physical origin, i.e., a large-scale rotation of the active region around the biggest sunspot.

Our results indicate that the flux of the field lines created by magnetic reconnection and the magnetic helicity generated by the shear flow may be much more than enough for the formation of the filament. This means that the magnetic structure created during evolution must be much bigger than the newly formed filament. Further comparison of magnetic flux and magnetic helicity strongly suggests that the newly created magnetic structure may consist of a flux

rope inside which the filament is embedded and a sheared coronal arcade that overlies the flux rope. This suggestion is consistent with the current knowledge that a prominence exists in association with the larger coronal structures like coronal arcades (for a recent review, see Engvold 1998) and the picture that a prominence represents only a part, namely, the bottom portion, of a flux rope where cool plasma can be sustained against gravity (Priest, Hood, & Anzer 1989; Ridgway & Priest 1993). Interestingly, the new magnetic structure has magnetic flux and magnetic helicity that are of the same order of magnitude as those of an interplanetary magnetic cloud.

We appreciate the *SOHO*/MDI team's effort for providing the magnetograms. We thank the referee for critical comments and suggestions that helped in improving the manuscript. This work is supported in part by the US-Korea Cooperative Science Program (KOSEF 995-0200-002-2, NSF INT-98-16267), by NASA under grants NAG5-9682, NAG5-7837, NAG5-9501, by NSF under grant ATM 00-86999, and by the BK21 project of the Korean Government.

APPENDIX A

ERRORS IN GEOMETRIC CORRECTION

For simplicity and feasibility, we have assumed that magnetic field is vertical everywhere and have used the relation

$$B_l = B_z \cos \psi \quad (\text{A1})$$

to determine the vertical component B_z from the observed line-of-sight component B_l . The heliocentric angle ψ is related to the heliographic coordinates (b , l) of the location via the equation

$$\cos \psi = \cos b_0 \cos b \cos (l - l_0) + \sin b_0 \sin b, \quad (\text{A2})$$

where b_0 and l_0 represent the heliographic latitude and longitude of the disk center. In reality, this simple relation does not hold at the places where horizontal magnetic fields are strong, and the oversimplification may have produced nonnegligible errors in the measured vertical field strength, magnetic flux change, and helicity change. We now attempt to estimate these possible errors.

According to Gary & Hagyard (1990), the line-of-sight component of magnetic field, B_l , is generally given as a linear combination of the vertical field component B_z , the east-west component B_x , and the south-north component B_y ,

$$\begin{aligned} B_l = & [-\cos b_0 \sin (l - l_0)]B_x \\ & + [-\cos b_0 \sin b \cos (l - l_0) + \sin b_0 \cos b]B_y \\ & + [\cos \psi]B_z. \end{aligned}$$

Thus, the error in B_z , $\epsilon(B_z)$, is given by

$$\begin{aligned}\epsilon(B_z) &\equiv \frac{B_l}{\cos \psi} - B_z \\ &= CB_x + DB_y,\end{aligned}$$

with

$$\begin{aligned}C &= \frac{-\cos b_0 \sin(l - l_0)}{\cos \psi}, \\ D &= \frac{-\cos b_0 \sin b \cos(l - l_0) + \sin b_0 \cos b}{\cos \psi}.\end{aligned}$$

In August 1999, $b_0 = 6.7^\circ$. The center of the active region has the coordinates $b = 21^\circ$ for all the days and $l - l_0 = -47^\circ$ on August 16, -34° on August 17, -20° on August 18, and -7° on August 29. Therefore, the errors at the four different times are explicitly given as

$$\begin{aligned}\epsilon(B_z) &= 1.08B_x - 0.20B_y \text{ on August 16,} \\ \epsilon(B_z) &= 0.98B_x - 0.22B_y \text{ on August 17,} \\ \epsilon(B_z) &= 0.37B_x - 0.25B_y \text{ on August 18,} \\ \epsilon(B_z) &= 0.13B_x - 0.25B_y \text{ on August 19.}\end{aligned}$$

The fake magnetic flux in a given area is given by

$$F_\epsilon \equiv \int \epsilon(B_z) dS = \int CB_x dS + \int DB_y dS. \quad (\text{A3})$$

Suppose B_x and B_y remain constant. Then the change of the net flux caused by the projection correction error between August 16 and 19 is given by

$$\begin{aligned}(\Delta F)_\epsilon &= -0.95 \int B_x dS - 0.05 \int B_y dS \\ &\approx -\langle B_x \rangle S.\end{aligned}$$

This relation shows that the fake change of magnetic flux in a given area arising from the projection correction error depends on the averaged east-west component of the horizontal magnetic field. For example, at regions where the horizontal field is strong enough and directed to the east ($B_x < 0$), the net flux may appear to increase with time.

APPENDIX B

FAKE MOTION DUE TO GEOMETRIC CORRECTION ERROR

The geometric correction error of B_z may produce apparent motion of flux elements in the east-west direction (x -direction) due to solar rotation. Suppose a region where the projection error $\epsilon(B_z)$ dominates B_z , and hence $B_l/\cos \psi \approx \epsilon(B_z)$. Then, tracking $B_l/\cos \psi$ in this region reflects a fake motion due to geometric correction error. From the condition

$$\frac{d\epsilon(B_z)}{dt} = \left(\frac{dC}{dt} B_x + \frac{dD}{dt} B_y \right) + \left(C \frac{dB_x}{dx} \frac{dx}{dt} + D \frac{dB_y}{dx} \frac{dx}{dt} \right) = 0, \quad (\text{B1})$$

the velocity of the fake motion $v_\epsilon \equiv dx/dt$ is found to be

$$v_\epsilon = - \left(\frac{dC}{dt} B_x + \frac{dD}{dt} B_y \right) / \left(C \frac{dB_x}{dx} + D \frac{dB_y}{dx} \right), \quad (\text{B2})$$

with

$$\frac{dC}{dt} = \left\{ - \frac{\cos b_0 [\cos b_0 \cos b + \sin b_0 \sin b \cos(l - l_0)]}{\cos^2 \psi} \right\} \omega \quad (\text{B3})$$

and

$$\frac{dD}{dt} = \left(\frac{\cos b_0 \sin b_0 \sin l}{\cos^2 \psi} \right) \omega, \quad (\text{B4})$$

where ω is the angular speed of solar rotation given in equation (1).

Thus, the velocity of the fake motion on different days is explicitly given as

$$v_{\epsilon} = \omega \frac{4.27B_x + 0.19B_y}{1.08B'_x - 0.20B'_y} \text{ on August 16 ,} \quad (\text{B5})$$

$$v_{\epsilon} = \omega \frac{2.97B_x + 0.10B_y}{0.68B'_x - 0.22B'_y} \text{ on August 17 ,} \quad (\text{B6})$$

$$v_{\epsilon} = \omega \frac{2.34B_x + 0.05B_y}{0.37B'_x - 0.25B'_y} \text{ on August 18 ,} \quad (\text{B7})$$

where $B'_x = dB_x/dx$ and $B'_y = dB_y/dx$. For simplicity, if it is assumed that $B_y = 0$ at the polarity reversal boundary, it follows that

$$v_{\epsilon} \approx f\omega L \operatorname{sgn}(B_x B'_x) , \quad (\text{B8})$$

where f is a factor ranging from 4 to 6 and L is the scale length of B_x . If we set L to be equal to half of the radius of the sunspot, 15,000 km, v_{ϵ} becomes about 0.2 km s^{-1} , which is not a negligible amount. However, serious fake motion is confined to small areas where magnetic fields are almost horizontal.

REFERENCES

- Berger, M. A. 1999, in *Magnetic Helicity in Space and Laboratory Plasmas*, ed. M. C. Brown, R. C. Canfield, & A. A. Pevtsov (Geophysical Monograph 111; Washington: American Geophysical Union), 1
- Chae, J. 2000, *ApJ*, 540, L115
- Chae, J., Denker, C., Spirock, T. J., Wang, H., & Goode, P. R. 2000, *Sol. Phys.*, 195, 333
- Choe, G. S., & Lee, L. C. 1992, *Sol. Phys.*, 138, 291
- DeVore, C. R. 2000, *ApJ*, 539, 944
- DeVore, C. R., & Antiochos, S. K. 2000, *ApJ*, 539, 954
- Engvold, O. 1998, in *IAU Colloq. 167, New Perspectives on Solar Prominences*, ed. D. Webb, D. Rust, & B. Schmieder (ASP Conf. Ser. 150; San Francisco: ASP), 23
- Galsgaard, K., & Longbottom, A. W. 1999, *ApJ*, 510, 444
- Gary, G. A., & Hagyard, M. J. 1990, *Sol. Phys.*, 126, 21
- Harvey, K., & Harvey, J. 1973, *Sol. Phys.*, 28, 61
- Howard, R., & Labonte, B. J. 1981, *Sol. Phys.*, 74, 131
- Howard, R. F., Harvey, J. W., & Forgach, S. 1990, *Sol. Phys.*, 130, 295
- Kim, I. S., & Alexeyeva, I. V. 1994, in *ASP Conf. Ser. 68, Solar Active Region Evolution: Comparing Models with Observations*, ed. K. S. Balasubramaniam & G. W. Simon (San Francisco: ASP), 403
- Litvinenko, Y. E. 1999, *ApJ*, 515, 435
- Litvinenko, Y. E., & Martin, S. F. 1999, *Sol. Phys.*, 190, 45
- Litvinenko, Y. E., & Somov, B. V. 1994, *Sol. Phys.*, 151, 265
- Martin, S. F. 1998, *Sol. Phys.*, 182, 107
- Martin, S. F., Livi, S. H. B., & Wang, J. 1985, *Australian J. Phys.*, 38, 929
- November, L. J., & Simon, G. W. 1988, *ApJ*, 333, 427
- Priest, E., & Forbes, T. 2000, *Magnetic Reconnection: MHD Theory and Applications* (New York: Cambridge Univ. Press)
- Priest, E. R., Hood, A. W., & Anzer, U. 1989, *ApJ*, 344, 1010
- Priest, E. R., van Ballegoijen, A. A., & Mackay, D. H. 1996, *ApJ*, 460, 530
- Ridgway, C., & Priest, E. R. 1993, *Sol. Phys.*, 146, 277
- Scherrer, P. H., et al. 1995, *Sol. Phys.*, 162, 129
- Schrijver, C. J., Title, A. M., van Ballegoijen, A. A., Hagenaar, H. J., & Shine, R. A. 1997, *ApJ*, 487, 424
- van Ballegoijen, A. A., & Martens, P. C. H. 1989, *ApJ*, 343, 971
- Wang, H., Tang, F., Zirin, H., & Wang, J. 1996, *Sol. Phys.*, 165, 223
- Wang, J. 1996, *Sol. Phys.*, 163, 319
- Wallenhorst, S. G., & Topka, K. P. 1982, *Sol. Phys.*, 81, 33
- Zwaan, C. 1987, *ARA&A*, 25, 83